

The Crucial Role of Water in Shaping Low-Barrier Hydrogen Bonds

Michael T. Ruggiero and Timothy M. Korter

Department of Chemistry, Syracuse University, 1-014 Center for Science and Technology,
Syracuse, NY 13244-4100, United States

Supporting Information

CONTENTS:

Results

Structural Results S3

Table 1. Single crystal XRD determined Water_a tilt angle and O_{far}-H_{mal} bond distances. S4

Terahertz Spectroscopic Results S5

Table 2. Experimental THz linewidths for the MMT series. S5

Figure 1. Experimental and calculated THz vibrational spectra of MnMT. S6

Figure 2. Experimental and calculated THz vibrational spectra of FeMT. S7

Figure 3. Experimental and calculated THz vibrational spectra of CoMT. S8

Figure 4. Experimental and calculated THz vibrational spectra of NiMT. S9

Figure 5. Experimental and calculated THz vibrational spectra of ZnMT. S10

Figure 6. Mass-dependence of MnMT vibrational frequency. S11

Table 2. Calculated O_{far}-H_{mal}-O_{near} stretching frequencies. S11

Molecular Orbital Analysis S12

Figure 7. MnMT COOP diagram. S13

Figure 8. FeMT COOP diagram.	S14
Figure 9. CoMT COOP diagram.	S15
Figure 10. NiMT COOP diagram.	S16
Figure 11. ZnMT COOP diagram.	S17
LBHB Potential	S18
Figure 12. H_{mal} potential of ZnMT, ZnMT without water _b , and ZnMT without water _a .	S18
Additional Supplementary Data and Video	
Animation of the low-frequency vibration in MnMT	
Animation of the high-frequency vibration in MnMT	
Experimental CIF file for the five MMT species	
References	S19

I. Additional Structural Results

All five MMT species are isomorphic and crystallize in the triclinic $P\bar{1}$ space group, and contain a single formula unit in the unit cell ($Z=1$) (**Figure 1**). The original literature structure of MnMT¹ indicated it to be completely isomorphic with ZnMT.^{1,2} However, that data was found to be inaccurate by a later report, where the authors determined that the β angle was incorrect.³ The structure obtained for this work confirmed these observations.

The unit cell parameters and heavy-atom positions of the redetermined structures are in good agreement with the available literature data.^{1,2,4,5} An exception is CoMT, for which the literature structure contains multiple errors that are resolved by the high-quality diffraction data obtained here.²² The DFT geometry optimizations yielded excellent agreement with the experimental structure. For example, the average error in the ZnMT non-hydrogen covalent bond distances is 0.44% (with respect to the low-temperature X-ray structure). Of particular note is the correct modeling of the maleate C-O bond distances (average error of 0.36%). This indicates that the proper single and double bond character of the carboxylate groups has been achieved by the simulation, meaning the hydrogen atom position in the LBHB is also accurate.

While the heavy-atom positions are in agreement there exist systematic differences in the covalent bond lengths involving hydrogen, particular when comparing the ZnMT neutron diffraction structure to the XRD determined structure,⁴ but this variation is attributable to the imprecise nature of XRD for measuring hydrogen positions. Considering the X-H covalent bonds, only ZnMT has been studied using neutron diffraction and therefore is the only structure available with precise hydrogen positions to serve as a benchmark. The average error in the calculated ZnMT X-H bond distances are small (2.0%) when compared to the neutron data, meaning the simulations provide reliable hydrogen positional data.⁴ Given the high quality of the simulations, all discussed bond distances and angles involving hydrogen atoms refer to the solid-state DFT optimized positions.

The pair of water_a molecules exhibits significant tilting in ZnMT that is not present in MnMT. The angle of this tilt is defined by the angle between the line connecting the metal and water_a-oxygen, and the line bisector of the water_a H-O-H angle. In MnMT, the water_a tilt is 8.875°, with an O_{near}-Owater_a bond distance of 3.09 Å and an O_{near}…H-Owater_a angle of 102.47°, while in ZnMT these values are 41.602°, 2.78 Å, and 140.17°, respectively (Table 1). The experimental water_a tilt angles are also provided in Table 1, and while calculated values differ slightly, the trends are very similar. The average deviation in the calculated tilt angles is ~8°, which is less than the differences between the individual species. The second subtle deviation is observed in the LBHB of the maleate ligand, with MnMT exhibiting a slightly longer O_{far}-H bond than in ZnMT (**Table 1**).

Table 1. Single crystal XRD determined water_a tilt angles and O_{far} – H_{mal} bond distances for the MMT series.

Species	Experimental Water _a Tilt Angle (°)	Experimental O _{far} -H _{mal} Distance (Å)
MnMT	14.16	1.17
FeMT	17.25	1.00
CoMT	22.46	1.04
NiMT	37.57	0.97
ZnMT	31.49	1.02

II. Terahertz Spectroscopic Results

The terahertz and calculated low frequency vibrational spectra are provided in **Figures 1-5**. The simulated spectra have been convolved using Lorentzian lineshapes using empirical full-width half-maxima (FWHM) (**Table 3**). The lowest-frequency terahertz motion involves an antisymmetric translation of the metal cation and coordinated water molecules, with simultaneous rotation of the maleate ligands. The higher-frequency motion involves a rotation of the maleate ligands with concurrent bending of all four coordinated metal-water bonds (animations of the motions have been uploaded as .avi files). As first approximations, the observed frequency trends could be caused by mass or radius changes from the different metal cations, and both of these factors were explored. The metal mass dependence of the vibrational modes was examined by utilizing MnMT as a model system and substituting the manganese cation mass with the masses of the other four metal cations, then re-evaluating the eigenvalues of the mass-weighted Hessian matrix. The result (**Figure 6**) showed that increasing the mass of the metal cation decreases the vibrational frequencies, as expected from the $\frac{1}{\sqrt{\text{reduced mass}}}$ dependence. However, the actual experimental frequencies increase significantly with increasing metal mass. The influence of different metal sizes was investigated by performing a geometry optimization of ZnMT while fixing the unit cell volume to that of the MnMT crystal (volumes of 313.95 and 357.13 Å³ for ZnMT and MnMT, respectively), but allowing all lattice parameters, angles, and atomic positions to relax within this constraint. The resulting structure did not yield any significant changes, and the position of H_{mal} and water_a remained consistent with the unconstrained optimization. The vibrations obtained from this expanded volume test were at slightly lower frequencies than the original simulation, but the calculated shift was not nearly as much as the measured shift. For the first vibrational mode, a shift of -0.77 cm⁻¹ was provided from the expanded volume test, only 16% of the -4.79 cm⁻¹ shift observed experimentally. These

results indicate that metal mass and ionic radii can influence the terahertz vibrations, but they do not play a dominating role.

The dependence of the terahertz features on the water_a tilt angle also provides a possible explanation for the varying FWHM of the absorptions in the experimental spectra (**Table 2**). It has been shown that the vibrational lifetime (and thus, spectral linewidth) of the modes is inversely proportional to hydrogen bonding strength.⁷ The linearity of the hydrogen bond geometry between water_a and O_{near} is directly related to the water_a rotation angle, with the furthest from linear (weakest) in MnMT and closest to linear (strongest) in NiMT. Therefore it can be surmised that the increasing linewidths are a result of stronger hydrogen bonding networks.

Table 2. Experimental THz linewidths for the MMT series.

Species	Average THz Linewidth
MnMT	3.28
FeMT	3.58
CoMT	3.52
NiMT	6.95
ZnMT	4.92

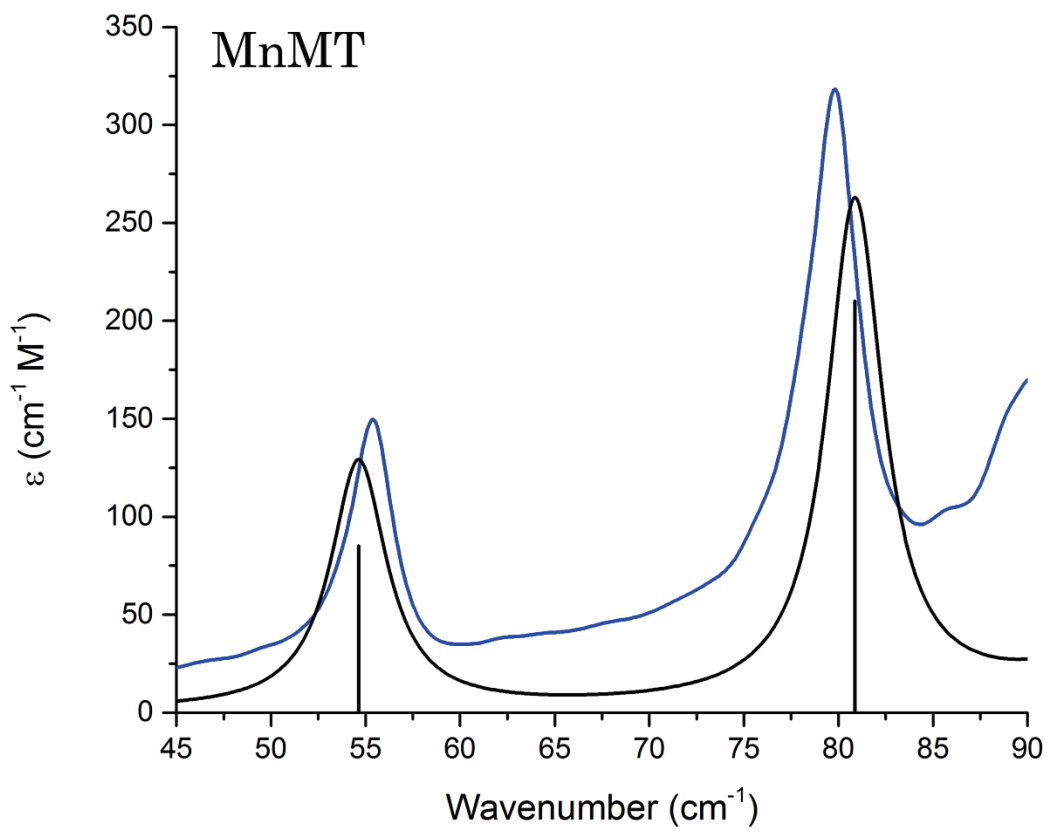


Figure 1. Experimental and calculated THz vibrational spectra of MnMT.

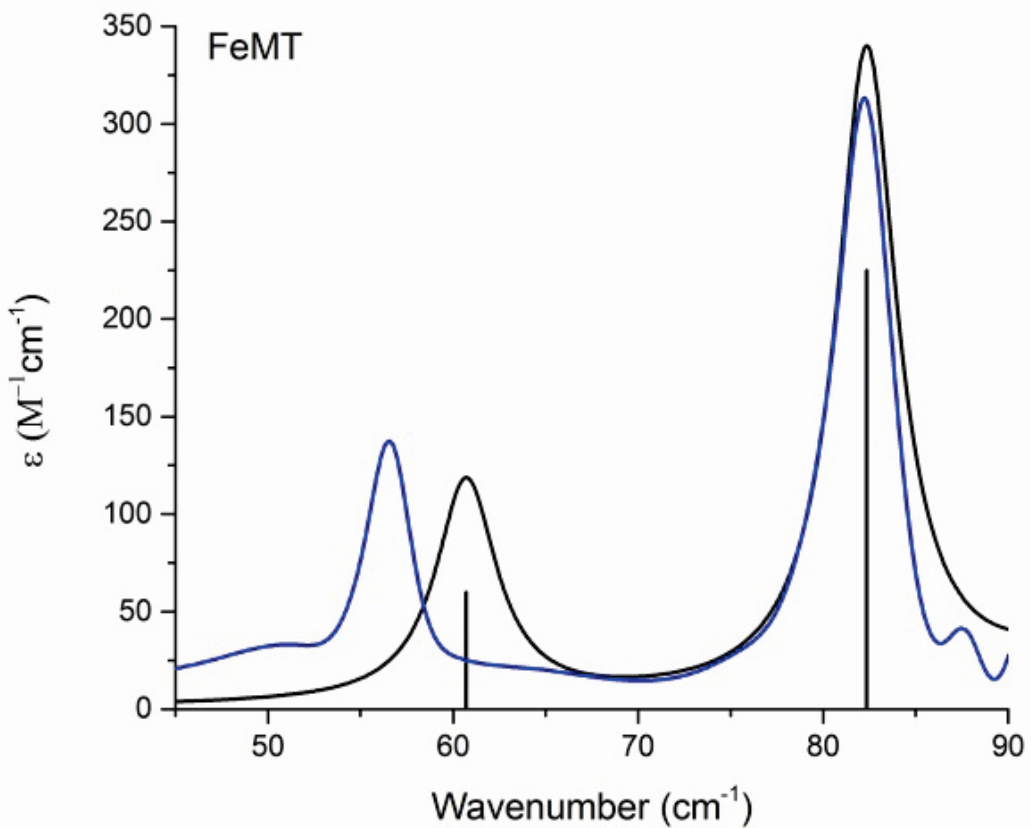


Figure 2. Experimental and calculated THz vibrational spectra of FeMT

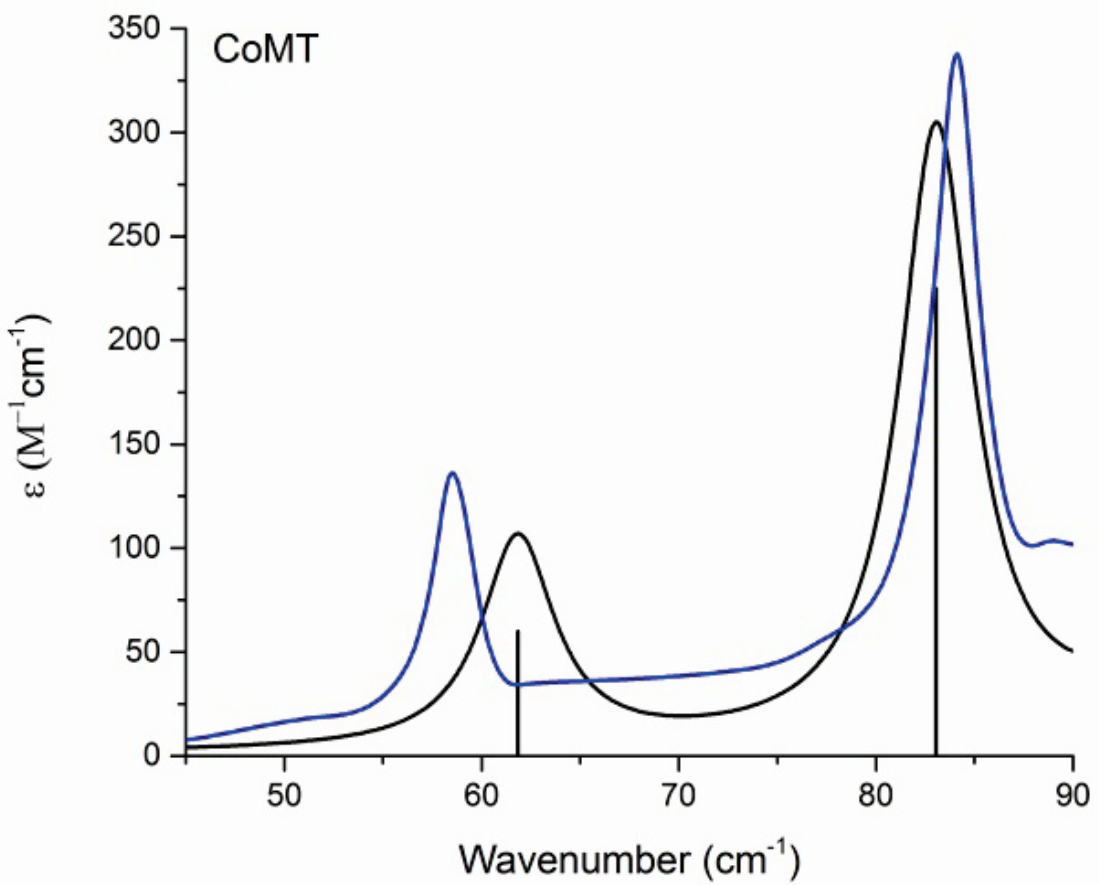


Figure 3. Experimental and calculated THz vibrational spectra of CoMT

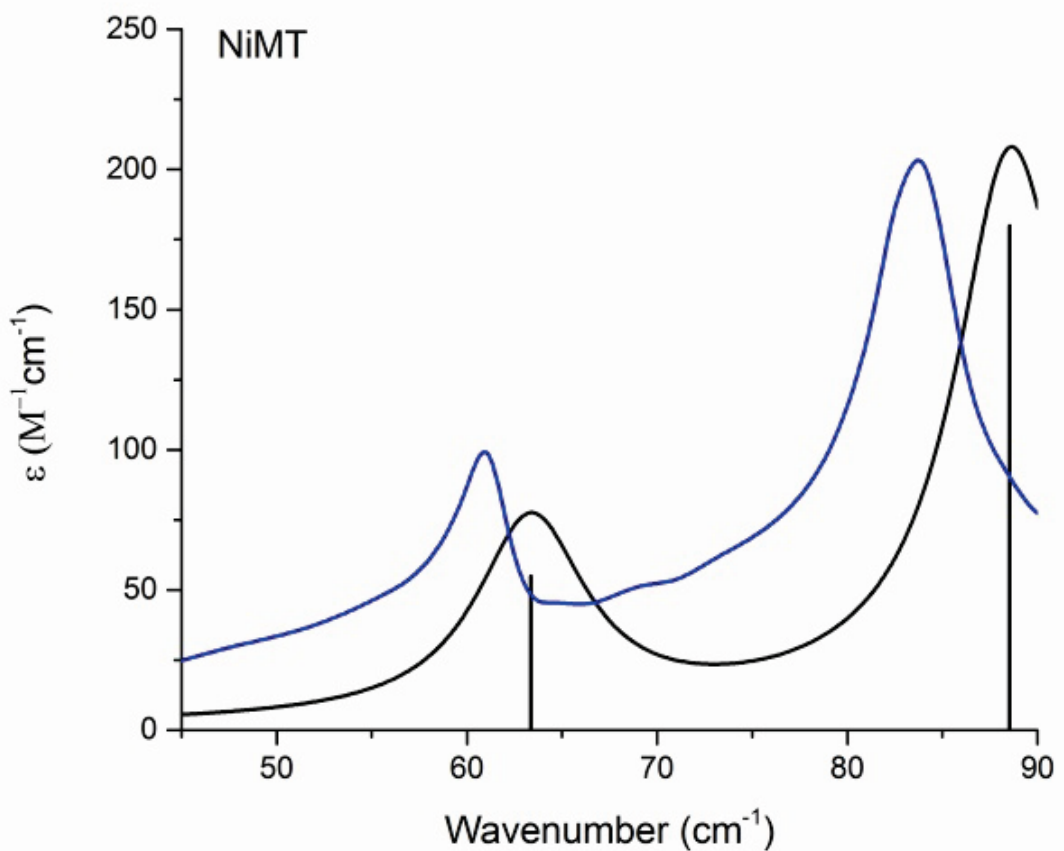


Figure 4. Experimental and calculated THz vibrational spectra of NiMT

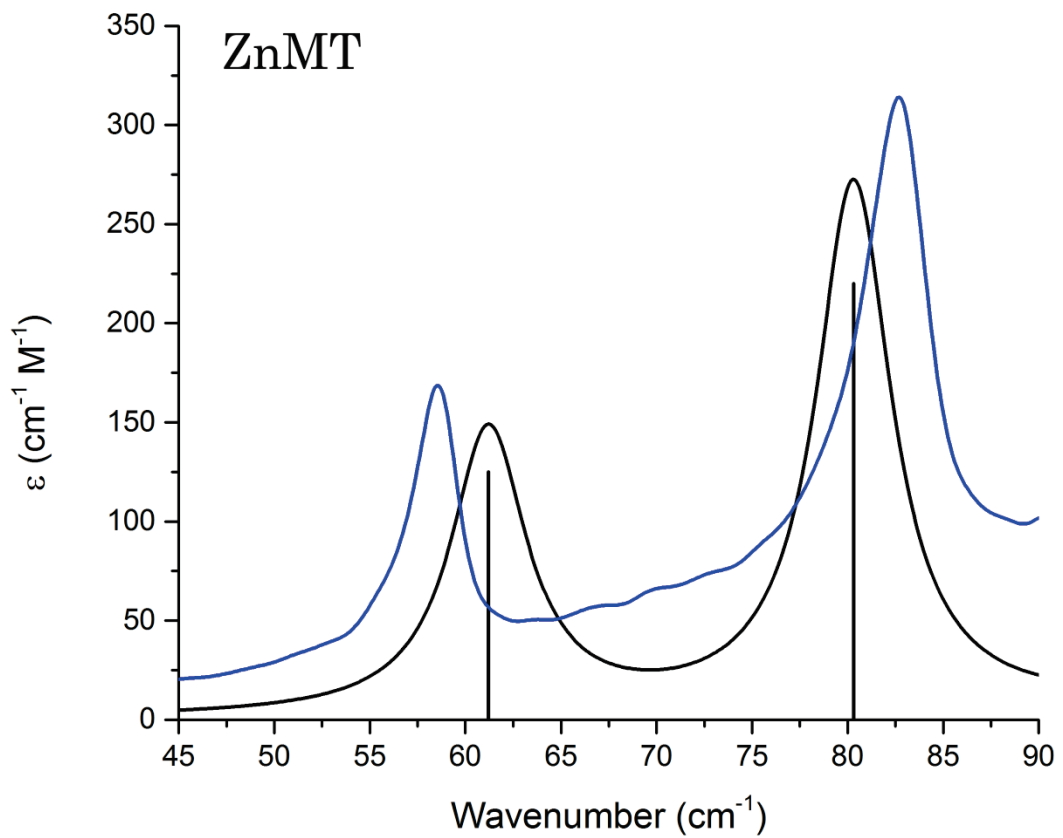


Figure 5. Experimental and calculated THz vibrational spectra of ZnMT

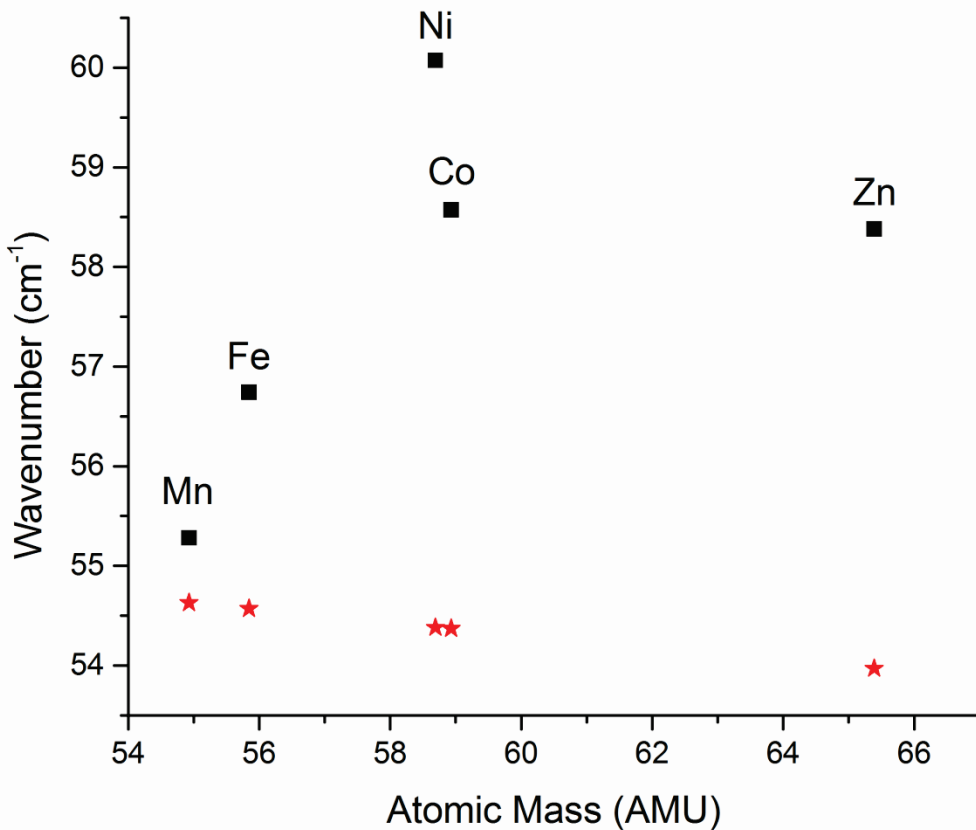


Figure 6. Calculated and experimental mass-dependence on vibrational frequency of MnMT

Table 2. Calculated O_{far}-H_{mal}-O_{near} stretching frequencies.

Species	Frequency (cm ⁻¹)
MnMT	1958.78
FeMT	2172.10
CoMT	2346.12
NiMT	2441.26
ZnMT	2417.86

III. Molecular Orbital Analyses

The solid-state optimized atomic positions were used as the basis for non-periodic calculations, where the isolated system under study was defined as a single crystallographic unit cell ($Z=1$): a metal cation, two maleate anions, and four water molecules. Rigid structures were used since all attempts to optimize the metal maleate formula units in the gas phase resulted in the loss of the solid-state structural features, even when clusters of up to nine formula units were tested. The isolated calculations were used to produce molecular orbitals, state densities, and the overlap matrices for every orbital present in the metal maleates, permitting detailed analysis of the spatial distribution of the electron density in each system.

A full analysis of the metal-water_a orbital overlap matrix was performed with specific attention given to the d -orbitals (the predominant variable across the transition metal series). To aid in the determination of the role of the individual metal d -orbitals involved in each molecular orbital, a Mulliken population analysis was also done for each species.⁸⁻¹¹ In agreement with the visual inspection of the molecular orbitals, the net overlap between the two species decreases as the metal-water_a angle increases. While total orbital overlap is useful for characterizing the metal-water_a interaction, it does not necessarily provide information regarding the specific populations of the molecular orbitals, such as bonding or antibonding character. In order to account for this, the overlap matrix elements must be weighted by the respective occupations of the molecular orbitals. This method is commonly referred to crystal orbital overlap population (COOP) analysis, and has been used in the past to characterize the interactions between fragments in molecular species.

The COOP analyses (**Figures 7-11**) provide detailed pictures regarding the nature of the chemical bond between the metals and water_a. For example, if only the orbital overlap was considered, MnMT and ZnMT would appear to be non-interacting because the bonding and antibonding interactions are equal, which is a result of the lack of crystal field stabilization energy typically attributed to d^5 and d^{10} metal-ligand interactions. However in the COOP diagrams, it is clearly shown that ZnMT and MnMT contain a larger proportion of bonding versus antibonding populations. In keeping with this approach, the total amount of bonding and antibonding populations were determined for each MMT by integration of the positive and negative regions of the COOP diagrams, respectively.

The antibonding population only slightly increases when moving from MnMT to FeMT, while there is a large increase in the total bonding population. This can be attributed to the increased overlap as well as the addition of an electron to the favorable d_{xz} orbital. This is further evidenced by the appearance of a positive peak on the FeMT COOP diagram. This peak disappears upon switching to CoMT, indicating that the next electron (added to one of the degenerate d_{xy} or d_{yz} orbitals) is involved in antibonding interactions. This causes water_a to tilt and ultimately results in relatively no change between the water_a-metal bond populations found in FeMT and CoMT.

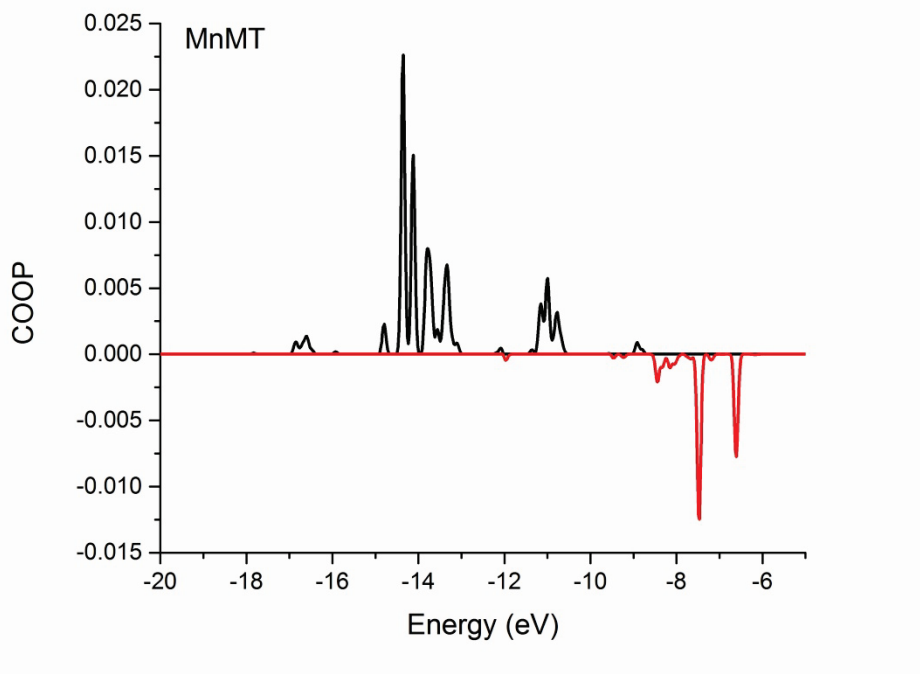


Figure 7. MnMT COOP diagram.

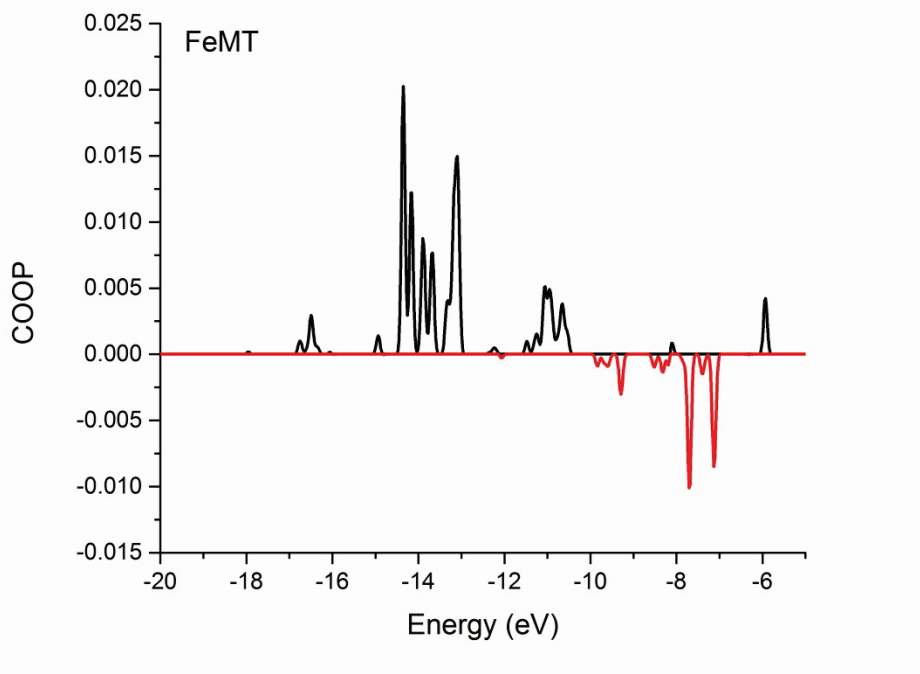


Figure 8. FeMT COOP diagram.

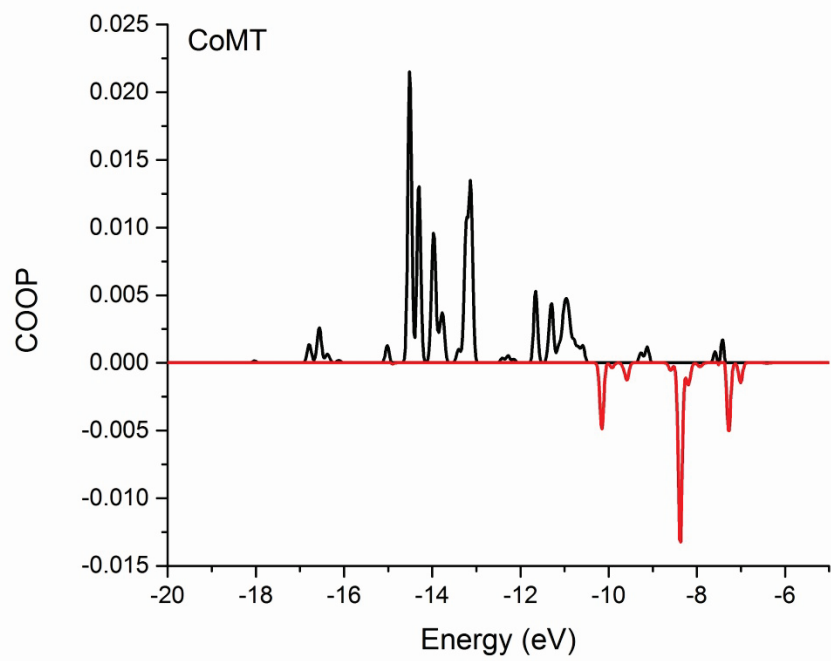


Figure 9. CoMT COOP diagram.

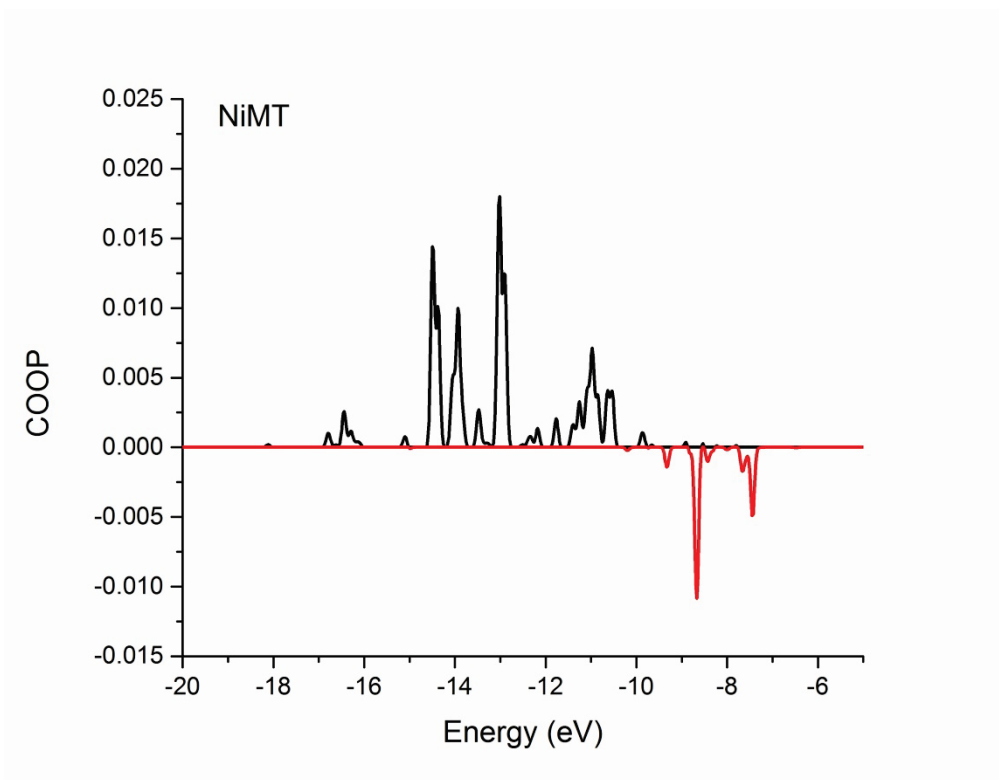


Figure 10. NiMT COOP diagram.

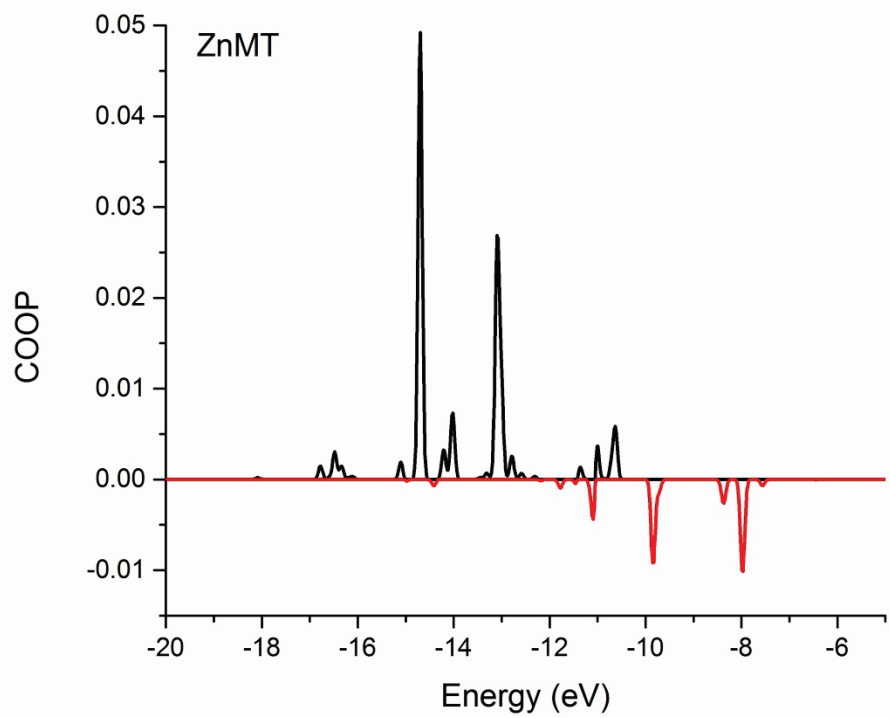


Figure 11. ZnMT COOP diagram.

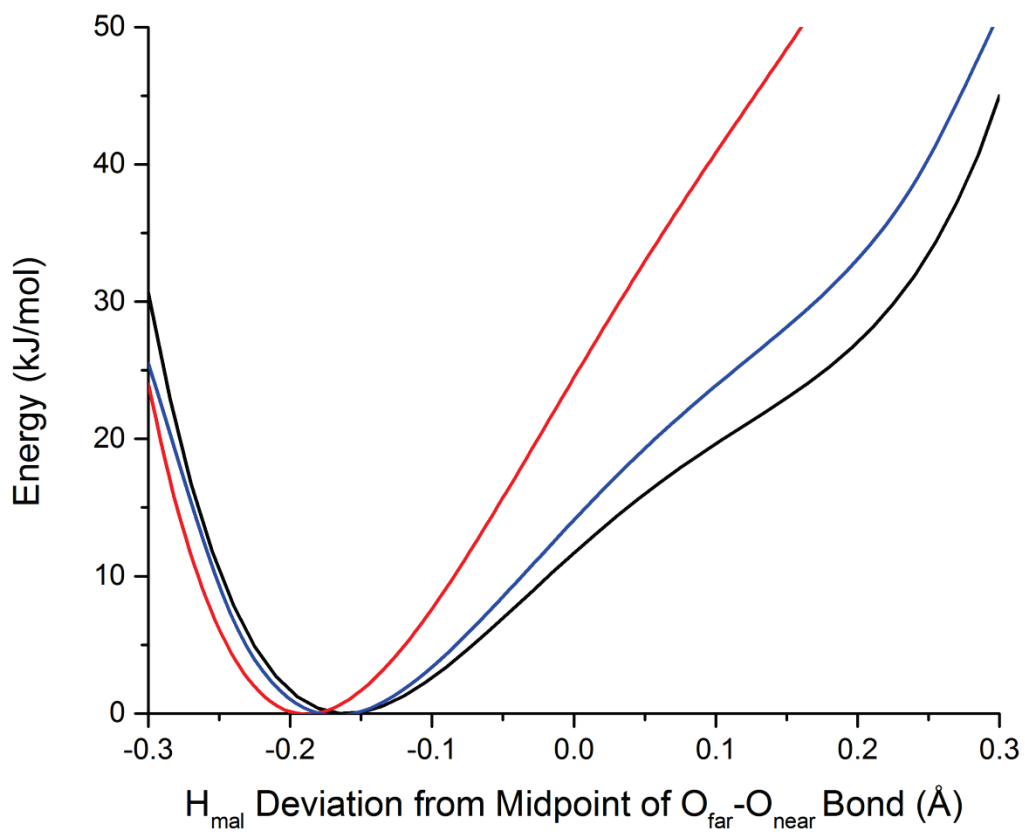


Figure 12. H_{mal} potential of ZnMT (black), ZnMT without water_b (blue), and ZnMT without water_a (red).

References

- (1) Gupta, M. P.; Geise, H. J.; Lenstra, A. T. H. *Acta Crystallogr., Sect. C: Cryst. Struct. Commun.* **1984**, *40*, 1152.
- (2) Gupta, M. P.; Mahanta, B. *Cryst. Struct. Commun.* **1978**, *7*, 179.
- (3) Lis, T. *Acta Crystallogr., Sect. C: Cryst. Struct. Commun.* **1983**, *39*, 39.
- (4) Sequeira, A.; Rajagopal, H.; Gupta, M. P.; Vanhouteghem, F.; Lenstra, A. T. H.; Geise, H. J. *Acta Crystallogr., Sect. C: Cryst. Struct. Commun.* **1992**, *48*, 1192.
- (5) Barman, R. K.; Chakrabarty, R.; Das, B. K. *Polyhedron* **2002**, *21*, 1189.
- (6) Sheldrick, G. *Acta Crystallogr. Sect. A* **2008**, *64*, 112.
- (7) Hakey, P. M.; Allis, D. G.; Ouellette, W.; Korter, T. M. *J. Phys. Chem. A* **2009**, *113*, 5119.
- (8) Rice, A.; Jin, Y.; Ma, X. F.; Zhang, X. C.; Bliss, D.; Larkin, J.; Alexander, M. *Appl. Phys. Lett.* **1994**, *64*, 1324.
- (9) Zhang, X. C.; Ma, X. F.; Jin, Y.; Lu, T. M.; Boden, E. P.; Phelps, P. D.; Stewart, K. R.; Yakymyshyn, C. P. *Appl. Phys. Lett.* **1992**, *61*, 3080.
- (10) Wu, Q.; Litz, M.; Zhang, X. C. *Appl. Phys. Lett.* **1996**, *68*, 2924.
- (11) Dovesi, R.; Orlando, R.; Erba, A.; Zicovich-Wilson, C. M.; Civalleri, B.; Casassa, S.; Maschio, L.; Ferrabone, M.; De La Pierre, M.; D'Arco, P.; Noël, Y.; Causà, M.; Réat, M.; Kirtman, B. *Int. J. Quantum Chem.* **2014**, *114*, 1287.
- (12) Becke, A. D. *J. Chem. Phys.* **1993**, *98*, 5648.
- (13) Ruggiero, M. T.; Bardon, T.; Strlič, M.; Taday, P. F.; Korter, T. M. *J. Phys. Chem. A* **2014**, *118*, 10101.
- (14) Ruggiero, M. T.; Bardon, T.; Strlic, M.; Taday, P. F.; Korter, T. M. *Phys. Chem. Chem. Phys.* **2015**.
- (15) Krishnan, R.; Binkley, J. S.; Seeger, R.; Pople, J. A. *J. Chem. Phys.* **1980**, *72*, 650.
- (16) Mitin, A. V.; Baker, J.; Pulay, P. *J. Chem. Phys.* **2003**, *118*, 7775.
- (17) Noel, Y.; Zicovich-Wilson, C. M.; Civalleri, B.; D'Arco, P.; Dovesi, R. *Phys. Rev. B* **2001**, *65*, 014111.
- (18) Frisch, M. J.; Trucks, G. W.; Schlegel, H. B.; Scuseria, G. E.; Robb, M. A.; Cheeseman, J. R.; Scalmani, G.; Barone, V.; Mennucci, B.; Petersson, G. A.; Nakatsuji, H.; Caricato, M.; Li, X.; Hratchian, H. P.; Izmaylov, A. F.; Bloino, J.; Zheng, G.; Sonnenberg, J. L.; Hada, M.; Ehara, M.; Toyota, K.; Fukuda, R.; Hasegawa, J.; Ishida, M.; Nakajima, T.; Honda, Y.; Kitao, O.; Nakai, H.; Vreven, T.; Montgomery, J. A.; Peralta, J. E.; Ogliaro, F.; Bearpark, M.; Heyd, J. J.; Brothers, E.; Kudin, K. N.; Staroverov, V. N.; Kobayashi, R.; Normand, J.; Raghavachari, K.; Rendell, A.; Burant, J. C.; Iyengar, S. S.; Tomasi, J.; Cossi, M.; Rega, N.; Millam, J. M.; Klene, M.; Knox, J. E.; Cross, J. B.; Bakken, V.; Adamo, C.; Jaramillo, J.; Gomperts, R.; Stratmann, R. E.; Yazyev, O.; Austin, A. J.; Cammi, R.; Pomelli, C.; Ochterski, J. W.; Martin, R. L.; Morokuma, K.; Zakrzewski, V. G.; Voth, G. A.; Salvador, P.; Dannenberg, J. J.; Dapprich, S.; Daniels, A. D.; Farkas; Foresman, J. B.; Ortiz, J. V.; Cioslowski, J.; Fox, D. J. Wallingford CT, 2009.
- (19) Hughbanks, T.; Hoffmann, R. *J. Am. Chem. Soc.* **1983**, *105*, 3528.
- (20) Gorelsky, S. I.; Lever, A. B. P. *J. Organomet. Chem.* **2001**, *635*, 187.
- (21) Humphrey, W.; Dalke, A.; Schulten, K. *Journal of Molecular Graphics* **1996**, *14*,

(22) Porollo, N. P.; Aliev, Z. G.; Dzhardimalieva, G. I.; Ivleva, I. N.; Uflyand, I. E.; Pomogailo, A. D.; Ovanesyan, N. S. *Russ. Chem. Bull.* **1997**, *46*, 362.